Opto-Electronics Review

Numerical simulations of a simple refractive index sensor based on side-hole optical fibres

Michał Dudek[*], Kinga K. Köllő

Institute of Applied Physics, Military University of Technology, 2 gen. Sylwestra Kaliskiego St., 00-908 Warsaw, Poland

Article info	Abstract
	In this work the influence of the cavity parameters on optical losses of a simple intensity-based in-line refractive index sensor utilizing a micromachined side-hole fibre was studied by means of numerical simulations. To perform these simulations, the Authors used the finite-difference time-domain method. The proposed sensor setup consists of light source, micromachined optical fibre as a sensor head, and a detector which makes it low-cost and easy to build. The changes of the external refractive index can be, therefore, recovered by direct measurements of the transmitted intensity from which insertion loss values can be calculated. By changing geometry of the cavity micromachined into the side-hole optical fibre, it was possible to determine its influence on the final sensor sensitivity and measurements range. Based on the provided analysis of simulations results, a simple fibre optic sensor can be fabricated mainly for sensing external liquids refractive index for application in biochemistry or healthcare.

1. Introduction

In recent years, the fibre optic sensor (FOS) technology has grown tremendously. It has evolved from the laboratory research stage to numerous practical implementations. To cope with the ever-expanding fields of their possible applications, the design of FOSs, as well as the technology to obtain them, had to be improved [1]. Amid many possibilities of FOSs, the in-line sensors with microcavities inside fibres can be highlighted [2]. This kind of sensor allows to measure the desired physical parameter using, for instance, change in the refractive index (RI) of the medium the sensor is placed in. The in-line cavity sensing is an unusual method since it requires change in the geometry of the optical fibre core, which in normal conditions is inaccessible. This method, however, is associated with the need of micromachining of the optical fibre using, for example, a laser beam or chemical etching [3–5]. The geometry of the cavity itself can determine optical losses which are one of the most important parameters in this kind of sensors, as they can be directly measured in a straight-

forward way and translated into specific changes in the cavity environment – thus performing the role of a sensor. The external factor influencing the propagation in such sensors is the RI of the external material, therefore, its measurements are widely used in various fields, including. e.g., biochemical sensing [6, 7], medicine [8, 9], environmental monitoring [10, 11], and physics [12–14].

FOSs can be divided regarding the type of modulation. Intensity sensors measure the transmission or reflection of the light and may be located along the fibre [15] or at its end, also with additional microstructures such as, e.g., polymer microtips [16–18]. Interferometric sensors detect the phase change of a signal due to an optical path length change, however, they only allow relative measurements of a physical quantity [19–21]. Polarimetric sensors determine the state of the beam polarization which allows the measurement of an external physical field which changed the polarized modes propagation constant [22, 23]. Spectroscopic sensors are mostly based on broad-emission radiation sources in conjunction with optical spectrum analysers or filters [24].

One of a special kind of optical fibres are side-hole optical fibres which have air tunnels (usually two) at the

*Corresponding author at: michal.dudek@wat.edu.pl

opposite sides of the core [25]. Their undoubted advantage is the possibility to access separately one or both air holes from the outside – e.g., by means of aforementioned micromachining – allowing the external material to be close to the core, in which the light field is propagating, and thus influencing this propagation. Side-hole optical fibres are often used to develop sensors, either based only on these fibres or in connection with other single- or multi-mode optical fibres [26, 27]. Amid many possibilities of RI FOSs, this paper is mainly focused on a simple intensity-based in-line sensor utilizing a micromachined side-hole fibre.

2.   Techniques

The presented study was conducted using the finite-difference time-domain (FDTD) method which is a widely used full-wave technique for the approximate description of electromagnetic waves propagation, especially in systems in which the dimensions of the investigated structures are comparable to the wavelengths used in the simulations [28]. Simulations were conducted using the ANSYS/Lumerical FDTD – a commercial 3D FDTD solver. To obtain the electric and magnetic components of the optical field propagating in the simulated structure in consecutive etches, power monitors were used (a feature of the software) that measure both the electric and magnetic field during the simulation. To calculate the insertion loss (IL) and return loss (RL) mode, expansion monitors were used. The RL was calculated as a fraction of the reflected field that coupled back into the selected mode in the first part of a waveguide, while the IL was calculated as a fraction of the field coupled into the selected mode in the second part of the waveguide, according to equations below:

$$\mathrm{IL} = 10 \log_{10} \frac{P_I}{P_T} \qquad (1)$$

$$\mathrm{RL} = -10 \log_{10} \frac{P_R}{P_I} \,, \qquad (2)$$

where P_I is the power inserted into the system (input power), P_T is the power transmitted through the system (output power), and P_R is the power reflected back from the system in the input direction. The reflected power P_R is significantly lower than the input power P_I, so without the "–" sign, the expression for RL in (2) would have a negative value and according to Bird [29] all loss quantities expressed in decibels (dB) should be positive numbers.

The proposed design of a simple intensity-based sensor setup consists of a laser light source operating at a wavelength of 1550 nm, a micromachined side-hole optical fibre acting as a sensor head, which is spliced with two polarization maintaining single-mode fibres, and a light detector. This design is therefore low-cost and easy to construct, as no highly sophisticated devices, such as, e.g., optical spectrum analysers, are necessary. A scheme of this setup is presented in Fig. 1.

3.   Results

The studied structure was based on a custom-made side-hole optical fibre fabricated at the Optical Fiber Techno-
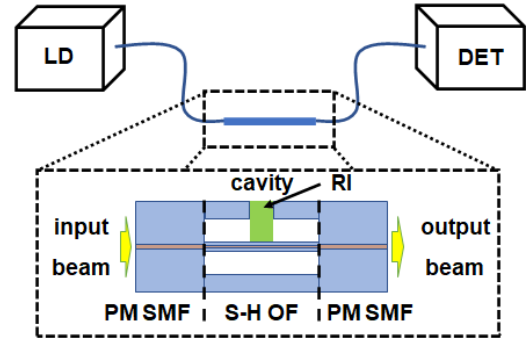

Fig. 1. Scheme of a porposed sensor design: LD – laser diode, DET – detector, PM SMF – polarization maintaining single-mode fibre, S-H OF – side-hole optical fibre, RI – external refractive index.

logy Laboratory, University of Maria Curie-Skłodowska, in Lublin, Poland and its cross-section is presented in Fig. 2. The simplified model of this fibre used in numerical simulations had an elliptic core with diameters of 1.0 μm × 2.3 μm, a cladding with diameters of 62.5 μm, and two elliptic holes with diameters of 16 μm × 12 μm. The RI of the cladding was set to $n_{clad} = 1.4425$, the RI of the core was set to $n_{core} = 1.4570$, therefore the refractive index difference was equal to $\Delta n = 0.010$, while the RI of the background was set to $n = 1$. The light sources were the fundamental HE_{11}^{x} (with an electric field oscillating along the minor axis of the core) and HE_{11}^{y} (with an electric field oscillating along the major axis of the core) modes at a wavelength of 1550 nm, to compare the two orthogonal polarizations. The simulation region was of 130 μm × 130 μm × 50 μm with a uniform mesh step of 0.1 μm and perfectly matched layer (PML) boundaries. Notches were simulated inside the fibre along with the longer and the shorter axis of the core. The longer axis of the core is along the x direction, while the shorter axis is along the y direction, as seen in Fig. 2.
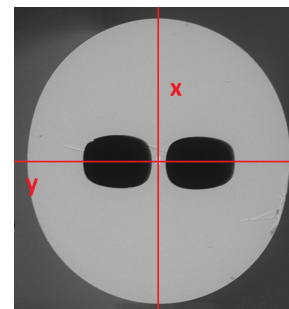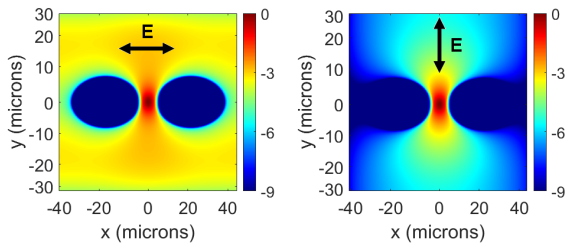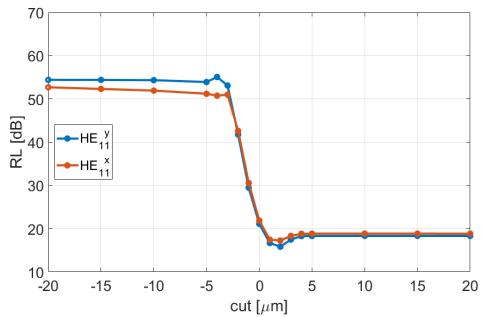

Fig. 2. Adopted coordinate system in the cross-section of the side-hole optical fiber.

The first series of simulations consisted of rectangular notches in the fibre with a width of 10 μm. A series of measurements with varying depths of notches was carried out in the optical fibre structure, from −20 μm (the reference point located in the centre of the core) to +20 μm. Intensities of the HE_{11}^{x} and HE_{11}^{y} mode profiles are visible in Fig. 3.
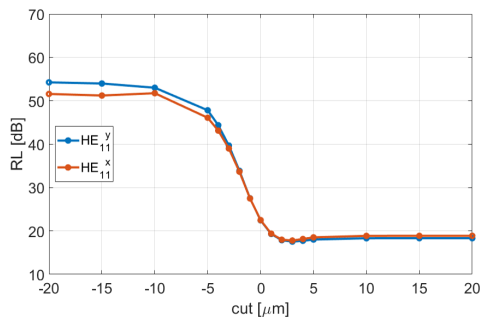
In all cases presented in Fig. 4, Fig. 5, Fig. 6, and Fig. 7. it is visible that the initial values of IL and RL, when the cut out did not influence the propagating modes yet, are at the level of about 0 dB and 54 dB, respectively. IL at 0 dB is perfectly normal for an unbroken optical fibre due to the
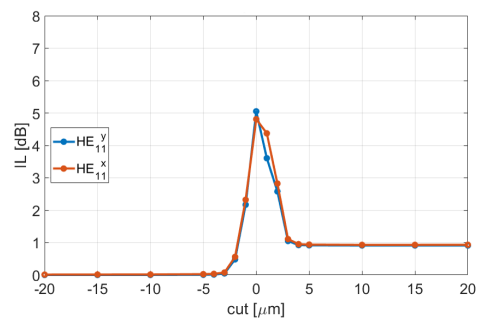
Fig. 3. Intensity of the HE_{11}^x mode profile (left) and HE_{11}^y mode profile (right) together with the directions of electric field oscillations denoted by E.
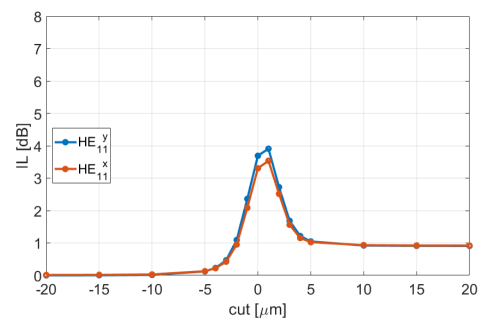

Fig. 4. Comparison of the RL of HE_{11}^x and HE_{11}^y modes in the rectangular notch simulated along the *x* axis.

Fig. 5. Comparison of the RL of HE_{11}^x and HE_{11}^y modes in the rectangular notch simulated along the *y* axis.
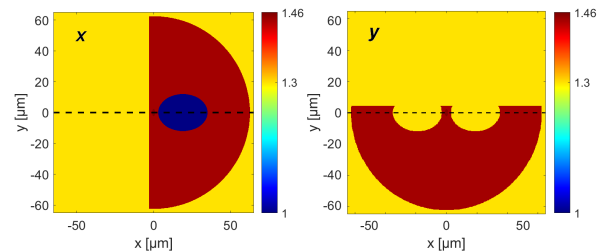

Fig. 6. The comparison of the IL of HE_{11}^x and HE_{11}^y modes in the rectangular notch simulated along the *x* axis

Fig. 7. Comparison of the IL of HE_{11}^x and HE_{11}^y modes in the rectangular notch simulated along the *y* axis.

homogeneous structure along the fibre major axis, while RL values at the level above 50 dB in this case represent back-reflection at the FDTD region border. Although the PML conditions were chosen during simulations, it evidently did not provide total evanescence of the fields propagating in the optical fibre core. Nevertheless, the simulations results are still perfectly valid and can be used to determine the properties of all modelled structures. The cut-outs are characterized by a high IL peak in regions where the core geometry is changed – the maximum loss occurs when the notch splits the core in the centre. In the cut-outs along the *y* axis, the IL peak is wider for both modes, as it starts at a cut-out depth of −5 μm, compared the cut-outs along the *x* axis, where the peak starts at a depth of −2 μm. This is directly caused by the ellipticity of the core having a radius of 1.0 μm × 2.3 μm which corresponds to the values of cut-out depths in which the peaks occur. Exceeding the peak, the IL values do not return to the initial ones after the introduction of the notches due to the fact that the light field scatters out of the optical fibre and propagates trough the medium (air) outside it before entering the other part of the optical fibre. RL in rectangular notches decreases with the notch depth, due to the increasing backscattering of light and stabilizes when the geometry changes no longer affect the core. The only difference between the notches made along the *x* and *y* axes is the slope of the RL characteristics.
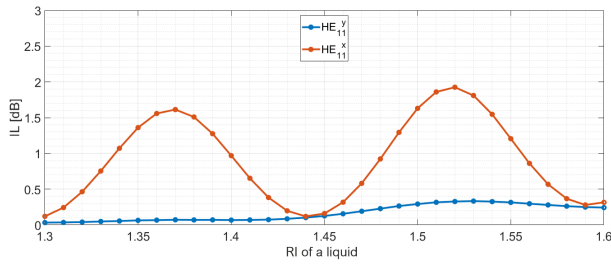
The above depicted results suggested a promising sensor application in notches ending close to the fibre core. For these cut-out depths, further simulations were performed, with a change in the external RI from 1.30 to 1.60 with a step of 0.01. The cross-sections of the structures can be seen in Fig. 8. First, the influence of the light beam polarization was examined. The HE_{11}^x and HE_{11}^y modes were simulated for cut-outs along both the *x* and *y* directions, with a notch end set to 2 μm from the core, as seen in Fig. 8. Subsequently, for a more prominent polarization plane, different distances from the core, different notch widths, and different core RIs were analysed. The diagrams of the simulation results have normalized both *x* and *y* axes for true comparison.
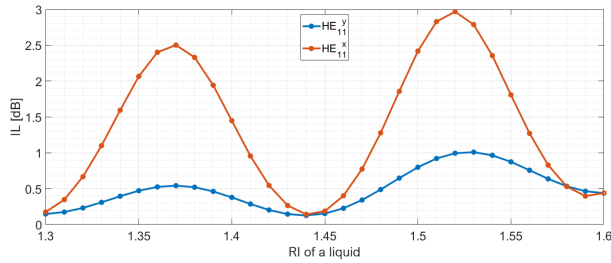

Fig. 8. Cross-section of the simulated structures with notches made along the *x* axis (left) and *y* axis (right).

The results of the simulations of HE_{11}^x and HE_{11}^y modes along the *x* and *y* axes are shown below, with a notch distance of 2 μm from the core boundary and a width of 10 μm. IL for each subsequent change of the surrounding RI is shown in Fig. 9 and Fig. 10.

As it can be seen in Fig. 3, the electric field intensity for the HE_{11}^x mode is visible enclosing the outer sides of the air tunnels in the fibre, while the field for HE_{11}^y mode is condensed mainly in the fibre core area. It can be deduced from the mode profile intensities, that the HE_{11}^x mode is,

Fig. 9. IL values of both the HE_{11}^x and HE_{11}^y modes in the simulated structures with 10 μm width notches made along the *x* axis with a 2 μm distance from the core.

Fig. 10. IL values of both the HE_{11}^x and HE_{11}^y modes in the simulated structures with 10 μm width notches made along the *y* axis with a 2 μm distance from the core.

Fig. 11. IL values of the HE_{11}^x modes in the simulated structures with 10 μm width notches made along the *x* axis with three different distances from the core.

Fig. 12. IL values of the HE_{11}^x modes in the simulated structures with 10 μm width notches made along the *y* axis with three different distances from the core.

Fig. 13. IL values of the HE_{11}^x modes in the simulated structures with three different widths of notches made along the *x* axis with a 2 μm distance from the core.

Fig. 14. IL values of the HE_{11}^x modes in the simulated structures with three different widths of notches made along the *y* axis with a 2 μm distance from the core.
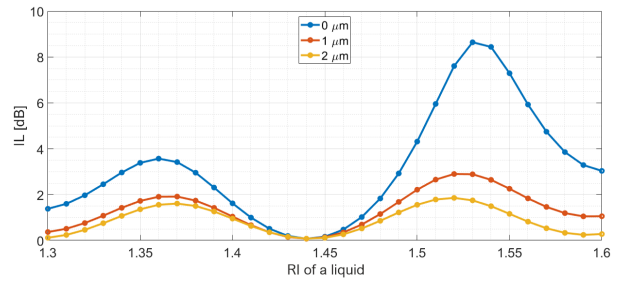
therefore, much more responsive to the changes of external RI since it covers a wider area of the fibre. This difference in the field intensity is confirmed in the diagrams above (Fig. 9 and Fig. 10), since it is visible that IL values for the HE_{11}^x mode are higher and have a higher responsivity than in case of the HE_{11}^y mode. It can also be deduced that the geometry of the fibre affects the responsivity, as well. In case of geometry in which both air tunnels affected by the RI change along *y* axis, IL changes have a higher peak-to-valley ratio than in case of notches along the *x* axis. Noteworthy is that there is also a visible change in IL of the HE_{11}^y mode which is much lower in the simulations along the *x* axis. For further simulations, the HE_{11}^x mode was chosen due to its wider range of changes depending on the changing RI.

The first parameter variations consisted of examination of three different distances from the core boundary: 0 μm, 1 μm, and 2 μm along both axes. The results of these simulations are shown in Fig. 11 and Fig. 12. Additionally, to the notch position, the notch width was investigated, as well. The width was set to 5 μm, 10 μm (initial one), and 20 μm. The results are presented in Fig. 13 and Fig. 14.
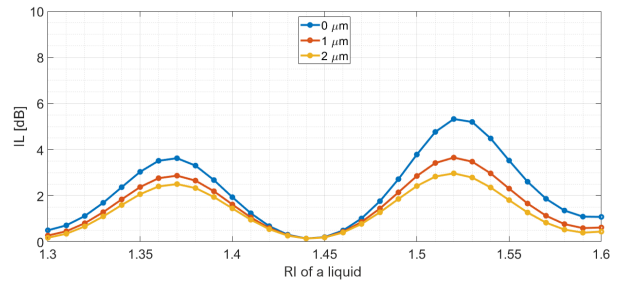
The last simulation variation concerned the variation of Δn which was changed from 0.010 to 0.015. These simulation results are shown in Fig. 15 and Fig. 16.

The simulations results of the HE_{11}^x mode along the *x* and *y* axes, with different notch distances and a notch width of 10 μm are shown in Fig. 11 and Fig. 12. The cavity ends were set to 0 μm, 1 μm, and 2 μm from the core-cladding boundary.
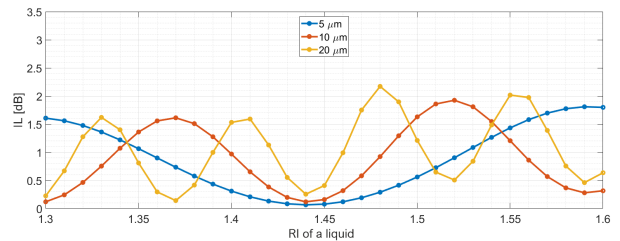
The maximum value of IL in simulations along the *y* axis are lower than for *x* axis. The IL values of the notch position set through the middle of the core are higher when the core is wider, since the scattering angle is higher in this case. It is visible that the values further from the core remain similar independently of the axis direction – the notches are positioned further from the core, so the core geometry no longer introduces such inequalities. The
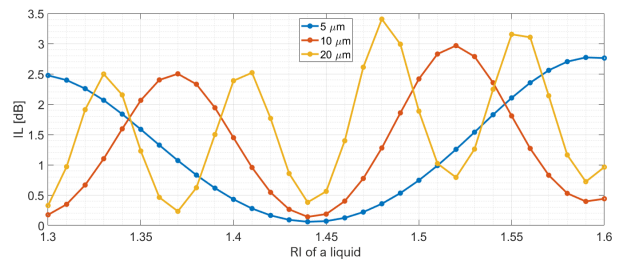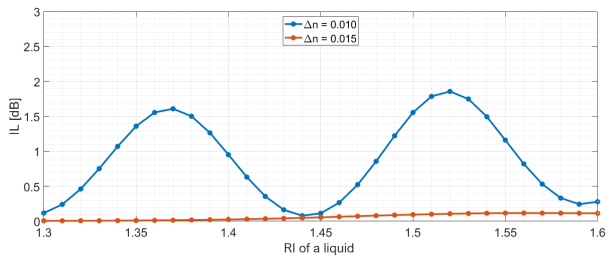
highest responsivity sensor would consist of a notch ending at the core-cladding boundary, made along the *x* axis. In this case, parts of the IL characteristics could be approximated by linear relations providing a linear response to the changes of external RI in desired ranges, in this case, e.g., 1.37–1.42 or 1.47–1.52. The possible RI measuring range has no dependence on distance from the core, so the only criterion in manufacturing a sensor with respect to the core distance would be sensor sensitivity.

The simulations results of the HE_{11}^x mode along the *x* and *y* axes, with a notch width set to 5 μm, 10 μm, 20 μm and a distance from the core-cladding boundary set to 2 μm are shown in Fig. 13 and Fig. 14.

Fig. 15. IL values of the HE_{11}^x modes in the simulated structures with 10 µm width notches made along the *x* axis with a 2 µm distance from the core and with two different values of Δ*n*.

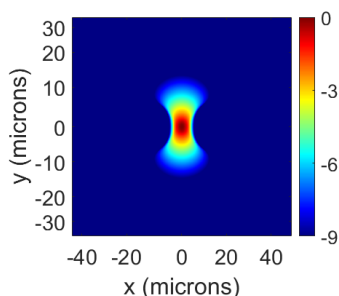
Fig. 16. IL values of the HE_{11}^x modes in the simulated structures with 10 µm width notches made along the *x* axis with a 2 µm distance from the core and with two different values of Δ*n*.

IL dependence on the notch width is similar regardless of the axis in which the geometry changes, although the loss values are higher in case of notches along the *y* axis. As mentioned before, it can be directly related to the ellipticity of the core. Additionally, IL curves presented in Fig. 13 and Fig. 14 indicate that when the notch is located near the core, the cut-out trough both holes results in a decisively higher response due to a larger area with the changed RI. In sensing applications, the notch width should be matched with the intended RI range measurements. In case of precise measurements in a relatively low RI range, a higher notch width (e.g., 20 µm) is more desirable, since the responsivity is higher. For wider RI range measurements, a lower notch width (e.g., 5 µm) is more desirable, since most of the IL characteristics can be approximated by a linear relation. However, in the latter case, the loss values do not increase as rapidly as for shorter widths, so the sensor dynamics are lower.

The simulations results of the HE_{11}^x mode along the *x* and *y* axes, with a different core refractive index of $n_{core} = 1.4645$, which leads to Δ*n* = 0.015, and with the notch located at a 2 µm distance from the core-cladding boundary and its width set to 10 µm, are shown in Fig. 15 and Fig. 16. In Fig. 17, the intensity of the electric field of the HE_{11}^x mode used in the simulations is shown.

Fig. 17. Intensity of the HE_{11}^x mode profile for a core RI equal to 1.4645 (Δ*n* = 0.015).

Comparing the intensity of the mode profiles of the optical fibre with Δ*n* = 0.010 and Δ*n* = 0.015, the difference is evident. In Fig. 3, the electric field is visible in the whole area of the fibre, while in Fig. 17, it is mainly in the area between the air tunnels–near the core. The IL response to the external refractive index difference corresponds to the reasoning made above. The response of the fibre with Δ*n* = 0.015 is significantly lower in both series of simulations, along the *x* and the *y* axes, as well. There is a slight difference in the results for the external RI above 1.45, however, the loss values are still below 0.5 dB. Similar to the previous results, the simulations for notches made along the *y* axis have higher values of losses than the ones for the *x* axis, due to both air tunnels being covered in the external RI.

It is evident that for the intensity sensor to be reliable, the side-hole optical fibre should be weakly-guiding – in the presented case for Δ*n* = 0.010. In this case, a greater portion of the mode area resides within the cladding (mainly as evanescent tails of the guided mode) and the external RI strongly influences the propagating mode.

4. Conclusions

In this work, the influence of the cavity parameters on optical losses of a simple intensity-based in-line RI sensor utilizing the micromachined side-hole fibre was studied. After analysing the rectangular notches for both linear polarization modes for different RI values, the HE_{11}^y mode (oscillating along the major axis of the core) was rejected because of its lower responsivity regarding the RI change in comparison to the HE_{11}^x mode (oscillating along the minor axis of the core). This is directly connected with the fact that the electric field intensity in the HE_{11}^y mode is concentrated in the fibre core area, while in the HE_{11}^x mode it is distributed in the whole area of the side-hole fibre, also enclosing air tunnels. The comparison of the influence of core and notch distance on IL in notches along *x* and *y* axes showed that while the core geometry influences the losses when the notch is in close distance to it, with the increasing core-notch distance, the influence decreases. Therefore, in case of cavities along the *x* axis, there is no need to micromachine the cladding further than the air tunnel boundary, and in case of cavities along *y* axis, any arbitrary notch distance from the core provides similar IL sensitivity. Also, depending on the type of a desired sensing mode, a sensor with higher RI range and lower sensitivity or higher sensitivity in lower RI range can be obtained, based on the width of the cavity. Moreover, for the proposed intensity sensor to be reliable, the side-hole optical fibre should be weakly-guiding for the propagating mode to enclose the air tunnels. Based on the provided analysis of the simulations results, a simple intensity-based RI sensor utilizing the micromachined side-hole fibre can be fabricated mainly for sensing RI external liquids for application in biochemistry or healthcare. Since the measured IL values oscillate with changing RI values, *a priori* knowledge of the analysed fluid is necessary to properly fabricate the sensor for the specific range of RI changes to be measured. In this approach, each sensing head is designed to operate only in a fixed range of RI values. It makes the proposed sensor a versatile device for measurements of the changes in external RI fabricated according to the specific application.

Authors' statement

Acknowledgements

References

[1] Grattan, K. T. V. & Sun, T. Fibre optic sensor technology: an overview. *Sens. Actuator A Phys.* **82**, 40–61 (2000). https://doi.org/10.1016/S0924-4247(99)00368-4

[2] Zhou, X., Zhang, L. & Pang, W. Performance and noise analysis of optical microresonator-based biochemical sensors using intensity detection. *Opt. Express* **24**, 18197–18208 (2016). https://doi.org/10.1364/OE.24.018197

[3] Rao, Y.-J. & Ran, Z.-L. Optic fibre sensors fabricated by laser-micromachining. *Opt. Fiber Technol.* **19** 808–821 (2013). https://doi.org/10.1016/j.yofte.2013.07.016

[4] Wang, Y., Liao, C. R. & Wang, D. N. Femtosecond laser-assisted selective infiltration of microstructured optical fibres. *Opt. Express* **18**, 18056–18060 (2010). https://doi.org/10.1364/OE.18.018056

[5] Pallarés-Aldeiturriaga, D., Roldán-Varona, P., Rodríguez-Cobo, L. & López-Higuera, J. M. Optical fibre sensors by direct laser processing: A review. *Sensors* **20**, 6971 (2020). https://doi.org/10.3390/s20236971

[6] Kumar, A., Pankaj, V. & Poonam, J. Refractive index sensor for sensing high refractive index bioliquids at the THz frequency. *J. Opt. Soc. Am. B* **38**, F81–F89 (2021). https://doi.org/10.1364/JOSAB.438367

[7] Pérez, M. A., González, O. & Arias, J. R., Optical Fibre Sensors for Chemical and Biological Measurements. in *Current Developments in Optical Fibre Technology* (eds. Harun, S. W. & Arof, H.) (IntechOpen, 2013). https://doi.org/10.5772/52741

[8] Liu, P. Y. *et al.* Cell refractive index for cell biology and disease diagnosis: Past, present and future. *Lab Chip* **16**, 634–644 (2016). https://doi.org/10.1039/C5LC01445J

[9] Leal-Junior, A. G. *et al.* Polymer optical fibre sensors in healthcare applications: A comprehensive review. *Sensors* **19**, 3156 (2019). https://doi.org/10.3390/s19143156

[10] Yan, X., Li, H. & Su, X. Review of optical sensors for pesticides. *Trends Analyt. Chem.* **103**, 1–20 (2018). https://doi.org/10.1016/j.trac.2018.03.004

[11] Joe, H. E., Yun, H., Jo, S.-H., Jun, M. B. G. & Min, B.-K. A review on optical fibre sensors for environmental monitoring. *Int. J. Pr. Eng. Man-Gt.* **5**, 173–191 (2018). https://doi.org/10.1007/s40684-018-0017-6

[12] Costa, G. K. B. *et al.* In-fibre Fabry-Perot interferometer for strain and magnetic field sensing. *Opt. Express* **24**, 14690–14696 (2016). https://doi.org/10.1364/OE.24.014690

[13] Zhou, N. *et al.* MEMS-based reflective intensity-modulated fibre-optic sensor for pressure measurements. *Sensors* **15**, 2233 (2020). https://doi.org/10.3390/s20082233

[14] Pevec, S. & Donlagic, D. Multiparameter fibre-optic sensor for simultaneous measurement of thermal conductivity, pressure, refractive index, and temperature. *IEEE Photon. J.* **9**, 1–14 (2017). https://doi.org/10.1109/JPHOT.2017.2651978

[15] Stasiewicz, K. A., Jakubowska, I. & Dudek, M. Detection of organosulfur and organophosphorus compounds using a hexafluoro-butyl acrylate-coated tapered optical fibres. *Polymers* **14**, 612 (2022). https://doi.org/10.3390/polym14030612

[16] Pura, P. *et al.* Polymer microtips at different types of optical fibres as functional elements for sensing applications. *J. Light. Technol.* **3**, 2398–2404 (2015). https://doi.org/10.1109/JLT.2014.2385961

[17] Marć, P., Żuchowska, M. & Jaroszewicz, L. R. Reflective properties of a polymer micro-transducer for an optical fibre refractive index sensor. *Sensors* **20**, 6964 (2020). https://doi.org/10.3390/s20236964

[18] Marć, P., Żuchowska, M., Jakubowska, I. & Jaroszewicz, L. R. Polymer microtip on a multimode optical fibre as a threshold volatile organic compounds sensor. *Sensors* **22**, 1246 (2022). https://doi.org/10.3390/s22031246

[19] Tian, Z., Yam, S. S. H. & Loock, H. P. Refractive index sensor based on an abrupt taper Michelson interferometer in a single-mode fibre. *Opt. Lett.* **33**, 1105–1107 (2008). https://doi.org/10.1364/OL.33.001105

[20] Ran, Z., Rao, Z., Zhang, J., Liu, Z. & Xu, B. A Miniature fibre-optic refractive-index sensor based on laser-machined fabry–perot interferometer tip. *J. Light. Technol.* **27**, 5426–5429 (2009). https://doi.org/10.1109/JLT.2009.2031656

[21] Wei, T., Han, Y., Li, Y., Tsai, H. L. &. Xiao, H. Temperature-insensitive miniaturized fibre inline Fabry-Perot interferometer for highly sensitive refractive index measurement. *Opt. Express* **16**, 5764–5769 (2008). https://doi.org/10.1364/OE.16.005764

[22] Enokihara, A., Izutsu, M. & Sueta, T. Optical fibre sensors using the method of polarization-rotated reflection. *J. Light. Technol.* **5**, 1584–1590 (1987). https://doi.org/10.1109/JLT.1987.1075449

[23] Zheng, Y., Li, J., Liu, Y., Li, Y. & Qu, S. Dual-parameter demodulated torsion sensor based on the Lyot filter with a twisted polarization-maintaining fibre. *Opt. Express* **30**, 2288–2298, (2022). https://doi.org/10.1364/OE.448088

[24] Jin, W. *et al.* Recent advances in spectroscopic gas sensing with micro/nano-structured optical fibres. *Photonic Sens.* **11**, 141–157 (2021). https://doi.org/10.1007/s13320-021-0627-4

[25] Xie, H. M., Dabkiewicz, Ph., Ulrich, R. & Okamoto, K. Side-hole fibre for fibre-optic pressure sensing. *Opt. Lett.* **11**, 333–335 (1986). https://doi.org/10.1364/OL.11.000333

[26] Bao, L., Dong, X., Shum, P. P. & Shen, C. High sensitivity liquid level sensor based on a hollow core fibre structure. *Opt. Commun.* **499**, 127279 (2019). https://doi.org/10.1016/j.optcom.2021.127279

[27] Lin, H., Liu, F., Guo, H., Zhou A. & Dai, Y. Ultra-highly sensitive gas pressure sensor based on dual side-hole fibre interferometers with Vernier effect. *Opt. Express* **26**, 28763–28772 (2018). https://doi.org/10.1364/OE.26.028763

[28] Taflove, A. & Hagness, S. C. *Computational Electrodynamics – The Finite-Difference Time-Domain Method – 3rd Edition*. (Artech House, 2005). https://us.artechhouse.com/Computational-Electrodynamics-Third-Edition-P1929.aspx

[29] Bird, T. S. Definition and misuse of return loss [Report of the Transactions Editor-in-Chief]. *IEEE Antennas Propag. Mag.* **51**, 166–167 (2009). https://doi.org/10.1109/MAP.2009.5162049